


Anisotropic radiative heat transfer between nanoparticles mediated by a twisted bilayer graphene grating

Shui-Hua Yang , Yong Zhang *, Ming-Qian Yuan , Cheng-Long Zhou, and Hong-Liang Yi
*School of Energy Science and Engineering, Harbin Institute of Technology, Harbin 150001, People's Republic of China
 and Key Laboratory of Aerospace Thermophysics, Ministry of Industry and Information Technology,
 Harbin 150001, People's Republic of China*

 (Received 28 May 2021; revised 1 August 2021; accepted 30 August 2021; published 9 September 2021)

Twisted two-dimensional bilayers exhibit many intriguing physical phenomena through interlayer twisting and coupling. Manipulating the “twisted angle” between the two evanescently coupled layers enables the hybridization of polaritons, and the dispersion engineering of polaritons in these structures can be well controlled. In this paper, we study the near-field radiative heat transfer (NFRHT) between two nanoparticles in the presence of a bilayered hyperbolic metasurface, which is modeled as two arrays of graphene strips (GSs) in parallel. We prove that the topological transition of the surface state under different twisted angles [from open (hyperbolic) to closed (elliptical) contours] has significant effect on NFRHT between nanoparticles. When both the integral and interlayer twisted angles are adjusted to proper values, the bilayered GS can canalize the energy transmission channel of the nanoparticles, hence significantly amplifying the NFRHT. A modulation factor beyond five orders of magnitude is achieved. We also demonstrate that, when the nanoparticles are arranged in different directions along the twisted bilayered system, NFRHT between nanoparticles can be strongly enhanced or inhibited. By changing the chemical potential and filling factor of the twisted bilayered GS, NFRHT can be effectively modulated. This paper reveals a hybridization effect of polaritons on NFRHT between nanoparticles, giving a degree of freedom (twisted angle) for controlling the heat transfer at the nanoscale with potential for effective energy management.

DOI: [10.1103/PhysRevB.104.125417](https://doi.org/10.1103/PhysRevB.104.125417)

I. INTRODUCTION

The contribution of photon heat tunneling can amplify near-field radiative heat transfer (NFRHT) by several orders of magnitude compared with the blackbody limit governed by the Stefan-Boltzmann law [1–4], especially when the surface supports both surface phonon polaritons and surface plasmon polaritons (SPPs) [5–7]. The enhancement and further regulation of NFRHT opens the door to various applications like thermal rectifiers [8], thermal information memory [9], and near-field thermophotovoltaics [10]. Moreover, the development of fabrication of metamaterials results in extensive studies of the coupling of surface polaritons for NFRHT between metamaterials in theory, such as hyperbolic polaritons [11], magnetoplasmon polaritons [12], ellipse polaritons [13], and nonreciprocal polaritons [14]. Continuous efforts have been devoted to dominate photon tunneling and modulate NFRHT.

Merging the concept of bulk hyperbolic metamaterials and ultrathin metasurfaces has recently led to hyperbolic and extremely anisotropic σ -near-zero uniaxial metasurfaces [15–17]. In Ref. [17], authors analyzed the properties of topological transitions and the associated dramatic enhancement of light-matter interactions, allowing extreme confinement, easy access, processing, and radiation in dynamically reconfigurable directions. Recently, thanks to the pioneering work of Hu *et al.* [18,19], the hybridization of polaritons

has been successfully realized in bilayer or heterobilayered [two-dimensional (2D)] materials, in which one layer rotates relative to the other, resulting in fine control of the dispersion engineering of the polaritons. Polaritons in the bilayered system are allowed to propagate in both layers and then couple strongly with each other to form hybridized polariton modes [20,21]. In this way, electromagnetic wave dynamics inside the bilayers, which is governed by the isofrequency contour topology, can be tailored by adjusting the twist angles. Since the hybridization effect of polaritons can greatly change the optical performance of the system [22,23], i.e., altering the in-plane polariton propagations, we expect that the hybridization of polaritons can affect NFRHT.

A remarkable theoretical effort in this domain has been devoted to the study of the heat exchange between two or more nanoparticles [24–28]. The reduced particle size allows one to perform dipole approximation, where each particle is assumed to be a point source and interacts with the substrate [29–34]. The calculation can be simplified under this assumption. It has been shown that locating a metasurface near two nanoparticles can introduce a channel of propagating surface waves to assist the heat transfer [29–36]. The deterioration of thermal photon transport is delayed, especially at a long distance.

Inspired by the hybridization of polaritons, we use a twisted hyperbolic system, which supports the hybridization of hyperbolic SPPs (HSPPs), to modulate NFRHT between two nanoparticles. Specifically, we considered bilayered identical graphene strips (GS) separated by a dielectric spacer with a finite thickness. The effective medium theory (EMT) [17,37] based on the electrostatic method can be used to realize the

*Corresponding author: yong_zhang@hit.edu.cn

homogenization of these metasurfaces in the subwavelength approximation (the period is much smaller than the wavelength $L \ll \lambda$). It is shown that GS can support hyperbolic polaritons under appropriate structural parameters. Remarkably, we theoretically explored the topological transition of the polaritonic isofrequency curves from an open hyperbola-like curve to a closed circumferencelike one, giving rise to strongly directional and diffractionless propagation of hybrid HSPPs—canalization regime—along one specific in-plane direction and theoretically study the influence of this behavior on NFRHT between nanoparticles.

This paper is organized as follows. In Sec. II, we introduce the geometry of our system, provide the Green's function (GF) in the presence of the twisted bilayered structure, and give the expression of the heat transfer coefficient between two nanoparticles. In Sec. III, we discuss the optical properties of twisted bilayered GS and show the phenomenon of topological transformation as the interlayer twisted angle increases. In Sec. IV, we exhibit the modulation of heat transfer between nanoparticles by modifying the interlayer twisted angle. GF in the wave vector space and the local density of states in the spatial space at different interlayer twisted angles are adopted to understand the underlying physics of the results. In Sec. V, the coupling strength of nanoparticles along different directions of the hybrid HSPPs is discussed, and the canalization of energy transmission induced by the twisted bilayered GS is studied. Section VI is dedicated to the effects of the filling factors and the chemical potential. Finally, we give some concluding remarks in Sec. VII.

II. THEORETICAL ASPECTS

Let us consider a system composed of two nanoparticles (p_1 and p_2) and a bilayered identical periodic GS as shown in Fig. 1(a). The two nanoparticles with radius R are located above the GS with a particle-GS distance of d_z . The interparticle distance between the two nanoparticles is d_p . When $d_p > 3R$ and $d_z > 4R$, we can model dielectric nanoparticles as simple radiating electric dipoles [11,38]. The GS in each layer of the bilayered GS has a width of W and an air gap of G separating adjacent strips. We define bilayered GSs from top to bottom as GS1 and GS2, separated by a dielectric spacer with a thickness of d_G . Here, α and β are defined perpendicular to strip directions of the GS1 and the GS2, respectively. We define α as parallel to the x axis unless otherwise mentioned. When we twist the GS2 with respect to GS1 by an interlayer twisted angle of φ_L from 0° in Fig. 1(b) to 90° in Fig. 1(c), one can expect that the optical properties of the bilayered GS can be modulated, hence the NFRHT between nanoparticles. We assume that the two nanoparticles are always placed along the α axis unless otherwise mentioned. For simplicity, we assume the background and spacer materials to be vacuum, viz., $\epsilon_d = 1$. In addition to the theoretical study, we give a possible experimental realization of our configuration. The system discussed in this paper consists of the particle and surface; we thus can draw the experience from NFRHT measurements between sphere and flat plate which are well researched configurations [7,39–43]. For instance, Narayanaswamy *et al.* [42], Shen *et al.* [7], and Rousseau *et al.* [43] separately developed sensitive techniques to measure NFRHT between a

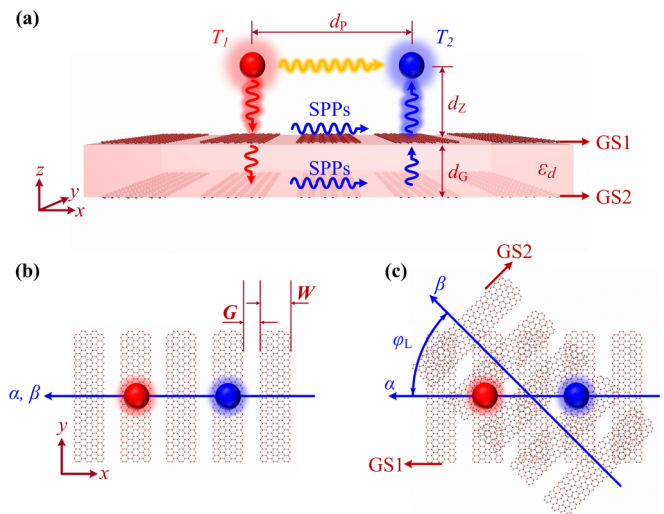


FIG. 1. Schematic of near-field heat transfer between two nanoparticles (p_1 and p_2) separated by an interparticle distance of d_p above the bilayered system. The twisted bilayered system is composed of two identical graphene strips (GSs; GS1 and GS2), where W and G are the strip width and air gap distance, respectively. GS1 and GS2 are separated by a thin dielectric spacer with a thickness of d_G and a dielectric constant of ϵ_d . d_z is the particle-GS distance for the two nanoparticles. (b) Top view of the particle-GS structure without twist. (c) Top view of the twisted particle-GS system at an interlayer twisted angle φ_L of with respect to the α axis.

microsphere and a substrate using the bimaterial atomic force microscope (AFM) cantilever. We thus could follow their ideas to develop an experimental setup for our configuration. The nanoparticles could be attached separately to the tips of biomaterial AFM cantilevers with ultraviolet (UV) adhesive. The base of the cantilever, the graphene sheets, the other particle, and the rest of the apparatus are approximately at the ambient temperature. Then a laser beam with a weak laser power is focused on p_1 to produce a tiny temperature increment. The bimaterial cantilever for p_2 bends because of a temperature increase caused by heat transfer between the two particles. This bending signal is detected interferometrically using a laser that is focused on the rear side of the cantilever and then is converted into heat transfer distance curves. In addition, we notice that the twisted bilayered GS can be realized experimentally by moiré nanolithography [44–46], which has the following procedures: First, we can apply multiple UV exposures through transparent photomasks at different angular offsets. It enables the massive production of subwavelength lattices. Interference lithography can also be used to fabricate moiré patterns without using photomasks, based on interference patterns between two or more coherent laser beams for one-dimensional and 2D moiré patterns.

We note that, by using the experimental methods given above, p_1 and p_2 as well as the bilayered structure could be kept at fixed temperatures T_1 , T_2 , and T_S , respectively. We assume that, except for p_1 whose temperature is $T + \Delta T$, the temperature of the entire system is fixed at temperature T ($T_2 = T_S = T$). Under this assumption, p_2 only has energy exchange with p_1 . When the temperature difference ΔT between two nanoparticles tends to zero, the heat transfer

coefficient h between the two nanoparticles can be determined. This is the quantity we discuss in this paper, especially focusing on how the presence of a twisted bilayered GS affects its change. We noticed that, due to the temperature difference between p_1 and the substrate, p_1 will also exchange part of the heat with the twisted bilayered structure, but this heat transfer will not affect the energy transferred from p_1 to p_2 . Therefore, in this paper, the bilayered GS purely acts as a boundary condition that can directly change the way of heat exchange between particles in vacuum.

The main point of this paper is to investigate the energy exchange between the two nanoparticles, and thus, the heat transfer between bilayered GS and the nanoparticles is not discussed here. A radiative heat transfer conductance (HTC) is defined to quantitatively evaluate the heat flux, which can be expressed in terms of the GF as [33]

$$h = 4 \int_0^{+\infty} \frac{d\omega}{2\pi} \hbar \omega k_0^4 n'(\omega, T) \chi^2 \text{Tr}(\mathcal{G}\mathcal{G}^\dagger), \quad (1)$$

where $k_0 = \omega/c$ is the wave vector in vacuum and $\chi(\omega) = \text{Im}[\alpha(\omega)] - k_0^3 |\alpha(\omega)|^2 / 6\pi$ denotes the electric polarizability of the particle. In the limit $R \ll \delta$ (where δ is the skin depth of the given material), the electric polarizabilities of the nanoparticles α are given by the well-known Clausius-Mossotti form [34,47]: $\alpha(\omega) = 4\pi R^3 \{[\varepsilon(\omega) - 1]/[\varepsilon(\omega) + 2]\}$, where $\varepsilon(\omega)$ is the dielectric function of the nanoparticles, $n'(\omega, T)$ denotes the derivative with respect to T of the Bose-Einstein distribution $n(\omega, T) = [\exp(\hbar\omega/k_B T) - 1]^{-1}$ and \dagger denotes the conjugate transpose. Here, \mathcal{G} denotes the dyadic Green's tensor of the full system, which is written in terms of Green's tensor as $\mathcal{G} = (I - k_0^4 \alpha_1 \alpha_2 \mathbb{G} \mathbb{G}^T)^{-1} \mathbb{G}$. It was reported that assistance of surface wave propagation causes a significant amplification of radiative heat transfer at distances ranging from near to far field. Note that the two nanoparticles investigated in Refs. [28,30,32–34] were placed on the same side of the plate, indicating that heat transfer amplification is attributed to surface waves reflected from the plate, where the interface acts as a wave guide. In this case, the interface reflection contribution plays a significant role in the heat transfer between nanoparticles. In the presence of a vacuum-material interface, the GF can be written as [48]

$$\mathbb{G} = \mathbb{G}_0 + \mathbb{G}_R, \quad (2)$$

where \mathbb{G} represents the contributions of the vacuum and the scattering part, accounting for direct particle-particle and particle-interface-particle channels, respectively. The scattering part depends on the interface reflections and goes to zero in the absence of the interface. In the infrared range, the effect of multireflection between the nanoparticles and the interface can be neglected. This is due to the existence of a radiative saturation mechanism for near-field heat exchange in many-body systems. This saturation arises because of thermalization of the interacting bodies when the separation d_z between the nanoparticles and interface is reduced. This mechanism has been discussed in detail in Ref. [49]. The vacuum contribution to the GF is given by

$$\mathbb{G}_0 = \frac{e^{ik_0 d_p}}{4\pi k_0^2 d_p^3} \begin{pmatrix} a & 0 & 0 \\ 0 & b & 0 \\ 0 & 0 & b \end{pmatrix}, \quad (3)$$

where $a = 2 - 2ik_0 d_p$, and $b = k_0^2 d_p^2 + ik_0 d_p - 1$.

The reflecting contribution of the multilayer metasurfaces to the electric-electric GF $\mathbb{G}_{R,EE}$ can be written as [50,51]

$$\begin{aligned} \mathbb{G}_{R,EE}(\mathbf{r}_i, \mathbf{r}_j, \omega) &= \frac{i}{8\pi^2} \int_{-\infty}^{\infty} dk_x \int_{-\infty}^{\infty} (r_{ss} \mathbf{M}_{ss} + r_{ps} \mathbf{M}_{ps} + r_{sp} \mathbf{M}_{sp} + r_{pp} \mathbf{M}_{pp}) \\ &\quad \times \exp[i[k_x(x_i - x_j) + k_y(y_i - y_j)]] \exp(ik_z |d_{z_i} + d_{z_j}|) dk_y, \end{aligned} \quad (4)$$

where the elements of the matrices \mathbf{M} along with the reflection coefficient in Eq. (4) are given as

$$\begin{aligned} \mathbf{M}_{ss} &= \frac{1}{k_z k_\rho^2} \begin{pmatrix} k_y^2 & -k_x k_y & 0 \\ -k_x k_y & k_x^2 & 0 \\ 0 & 0 & 0 \end{pmatrix}, \\ \mathbf{M}_{pp} &= \frac{k_z}{k_0^2 k_\rho^2} \begin{pmatrix} -k_x^2 & -k_x k_y & -\frac{k_x k_\rho^2}{k_z} \\ -k_x k_y & -k_y^2 & -\frac{k_y k_\rho^2}{k_z} \\ \frac{k_x k_\rho^2}{k_z} & \frac{k_y k_\rho^2}{k_z} & \frac{k_\rho^4}{k_z^2} \end{pmatrix}, \\ \mathbf{M}_{sp} &= \frac{1}{k_0 k_\rho^2} \begin{pmatrix} -k_x k_y & -k_y^2 & -\frac{k_y k_\rho^2}{k_z} \\ k_x^2 & k_x k_y & \frac{k_x k_\rho^2}{k_z} \\ 0 & 0 & 0 \end{pmatrix}, \\ \mathbf{M}_{ps} &= \frac{1}{k_0 k_\rho^2} \begin{pmatrix} k_x k_y & -k_x^2 & 0 \\ k_y^2 & -k_x k_y & 0 \\ -\frac{k_y k_\rho^2}{k_z} & \frac{k_x k_\rho^2}{k_z} & 0 \end{pmatrix}, \end{aligned} \quad (5)$$

where $k_\rho = \sqrt{k_x^2 + k_y^2}$ and $k_z = \sqrt{k_0^2 - k_x^2 - k_y^2}$ are the lateral and vertical wave vectors, respectively. Here, r_{ab} ($a, b = s, p$) is the Fresnel reflection coefficient, representing that an incoming a -polarized plane wave turns out to be an outgoing b -polarized wave. The reflection matrix \mathbf{R} is a 2×2 matrix in the polarization representation having the form

$$\mathbf{R}_m = \begin{bmatrix} r_{ss} & r_{sp} \\ r_{ps} & r_{pp} \end{bmatrix}. \quad (6)$$

In this paper, the reflection matrix can be obtained using a modified 4×4 transfer matrix method. The details are given in the Appendix.

III. OPTICAL PROPERTIES OF THE BILAYERED HYPERBOLIC METASURFACE

We choose nanoparticles made of silicon carbide (SiC), which is a typical polar dielectric material. The dielectric function is described using the Drude-Lorentz model [52]:

$$\varepsilon(\omega) = \varepsilon_\infty \frac{\omega_L^2 - \omega^2 - i\Gamma\omega}{\omega_T^2 - \omega^2 - i\Gamma\omega}, \quad (7)$$

with high-frequency dielectric constant $\varepsilon_\infty = 6.7$, longitudinal optical frequency $\omega_L = 1.83 \times 10^{14}$ rad/s, transverse optical frequency $\omega_T = 1.49 \times 10^{14}$ rad/s, and damping $\Gamma = 8.97 \times 10^{11}$ rad/s. From the electric polarizability, we obtain

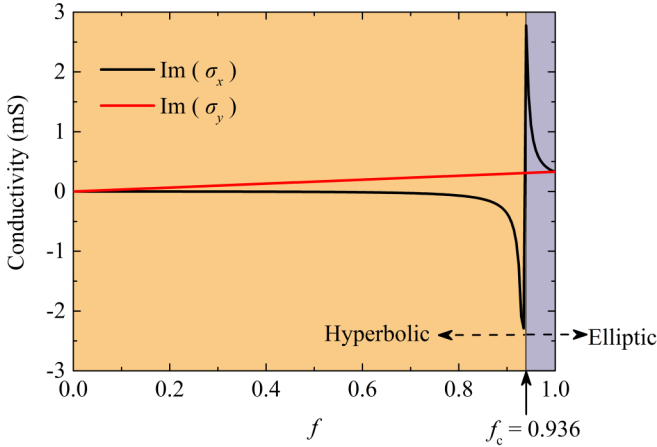


FIG. 2. Effective optical conductivity of graphene strip (GS) for different filling factors. Here, the unit of the surface conductivity is millisiemens (mS). The orange-shaded region denotes where $\text{sgn}(\text{Im}[\sigma_{xx}^{\text{eff}}]) \neq \text{sgn}(\text{Im}[\sigma_{yy}^{\text{eff}}])$, where hyperbolic graphene plasmons are supported.

a SiC nanoparticle resonance ω_{res} corresponding to the condition $\varepsilon(\omega) + 2 = 0$, which gives $\omega_{\text{res}} = 1.756 \times 10^{14}$ rad/s.

The optical conductivity of the GS can be analytically obtained using a well-known EMT as [17]

$$\sigma_{\text{eff}} = \begin{bmatrix} \sigma_{xx}^{\text{eff}} & 0 \\ 0 & \sigma_{yy}^{\text{eff}} \end{bmatrix} = \begin{bmatrix} \frac{P\sigma_G\sigma_C}{W\sigma_C + G\sigma_G} & 0 \\ 0 & \frac{W}{P}\sigma_G \end{bmatrix}, \quad (8)$$

where $\sigma_C = -i\omega\varepsilon_0 P / (\pi \ln[\text{csc}[0.5\pi(1-f)]])$ is an equivalent conductivity associated with the near-field coupling between adjacent strips obtained using an electrostatic approach. Here, P is the grating period equal to $W + G$, and f is the filling factor of the grating defined as W/P . This theory is valid when the strip periodicity P is far less than the wavelength of the plasmons, i.e., $P \ll \lambda_{\text{SPPs}}$ ($\sim 10 \mu\text{m}$ at room temperature). In addition, we note that the accuracy of the EMT might decrease when the nanoparticles are in the very near field of the GS. Thus, to guarantee the validity of the EMT for our calculations, the particle-GS distance d_Z should be several times greater than the strip periodicity. As detailed in Ref. [11], for $P = 20$ nm, the EMA predicts the real heat flux well when $d_Z \geq 60$ nm. Here, σ_G is the optical conductivity of the graphene sheet, and it is given by the well-known random phase approximation. Following Refs. [53,54], σ_G includes the contributions from both the intraband and interband transitions, i.e., $\sigma_G = \sigma_D + \sigma_I$, respectively:

$$\sigma_D = \frac{i}{\omega + \frac{i}{\tau}} \frac{2e^2 k_B T}{\pi \hbar^2} \ln \left(2 \cosh \frac{\mu}{2k_B T} \right),$$

$$\sigma_I = \frac{e^2}{4\hbar} \left[G \left(\frac{\hbar\omega}{2} \right) + i \frac{4\hbar\omega}{\pi} \int_0^\infty \frac{G(\xi) - G(\frac{\hbar\omega}{2})}{(\hbar\omega)^2 - 4\xi^2} d\xi \right]. \quad (9)$$

where $G(\xi) = \sinh(\xi/k_B T) / [\cosh(\mu/k_B T) + \cosh(\xi/k_B T)]$. Here, e is the electron charge, \hbar is the reduced Planck constant, μ is the chemical potential of GS, τ is the relaxation time and is fixed at 10^{-13} s for all the calculations, k_B is the Boltzmann constant, and ω is the angular frequency. Figure 2 shows the imaginary part of the conductivity of GS at $\mu = 0.5$ eV. The topology of the proposed structure may range

from open (hyperbolic) to closed (elliptical) as a function of its geometrical parameters and graphene characteristics, as revealed in Eq. (8). In the hyperbolic regime ($f < 0.936$), GS behaves as a metal ($\text{Im}[\sigma_{xx}^{\text{eff}}] > 0$) along one direction and as a dielectric ($\text{Im}[\sigma_{yy}^{\text{eff}}] < 0$) along the orthogonal one. The hyperbolic dispersion exhibited by GS in the hyperbolic region forces the HSPPs to propagate in the collimated direction. In turn, this feature provides an opportunity to adjust the evanescent coupling between two closely spaced GS. When both conductivity components have positive imaginary parts ($f > 0.936$), i.e., $\text{Im}[\sigma_{xx}^{\text{eff}}] > 0$ and $\text{Im}[\sigma_{yy}^{\text{eff}}] > 0$, elliptical anisotropic ($0.936 < f < 1.0$) and circular isotropic ($f = 1.0$) topologies can be achieved, thus supporting the induction surface for plasmon propagation in all directions. In this case, the energy is mainly focused in the direction with the lower imaginary conductivity component.

To provide further insight into the optical characteristics of the twisted bilayered GS, Figs. 3(b)–3(e) show the imaginary part of the TM reflection coefficient, viz., $\text{Im}[r_{pp}]$ at the nanoparticle resonance frequency of $\omega_{\text{res}} = 1.756 \times 10^{14}$ rad/s for the twisted bilayered structure with the interlayer twisted angles φ_L 0° , 30° , 60° , and 90° . The parameters of the GS are set as $f = 0.5$, $d_G = 10$ nm, and $\mu = 0.5$ eV. For comparison, we also show the case with bilayered unpatterned graphene sheets by setting $f = 1$, as depicted in Fig. 3(a). The dispersion relation curves obtained by Eq. (A8) are also denoted in the contour. We can see that the dispersion curves match well with the resonance region in the r_{pp} contour. This means that the hybrid SPP dispersion relations for the twisted bilayered system are well predicted by the reflection coefficients. When φ_L is 0° , we noticed that the hybrid HSPPs associated with GS1 and GS2 can interact with each other, resulting in two dispersion curves in a higher wave vector region (symmetric dispersion) and a smaller wave vector region (antisymmetric dispersion). As φ_L increases, the contour of the reflection coefficient exhibits from an open hyperbolalike to a closed circumferencelike pattern, experiencing a topological transition. The change of the hybrid HSPP propagation is attributed to polaritonic coupling between GS1 and GS2 in the twisted stack, giving rise to polaritonic propagation regimes, in comparison with monolayer GS. Note that, when $f = 1$, r_{pp} exhibits a circular topology, which indicates the isotropic propagation of SPPs in the bilayered graphene sheets, as shown in Fig. 3(a). Based on the above discussion, we can expect that the topology transition effect generated by an interlayer twist would have a great impact on NFRHT between the two nanoparticles.

IV. EFFECT OF HYBRID HSPPs ON HEAT TRANSFER BETWEEN NANOPARTICLES

To explore the effect of hybrid HSPPs on heat transfer at different interlayer twisted angles, in Fig. 4, we calculate the total HTC h as a function of interlayer twisted angle at a temperature of 300 K. The curves with different colors represent the result for different filling factors. The parameters of the bilayered GS are the same as Fig. 3. We place two nanoparticles at 60 nm above GS1, and the nanoparticles are placed along the α axis with a large interparticle distance of $d_p = 1 \mu\text{m}$ between them.

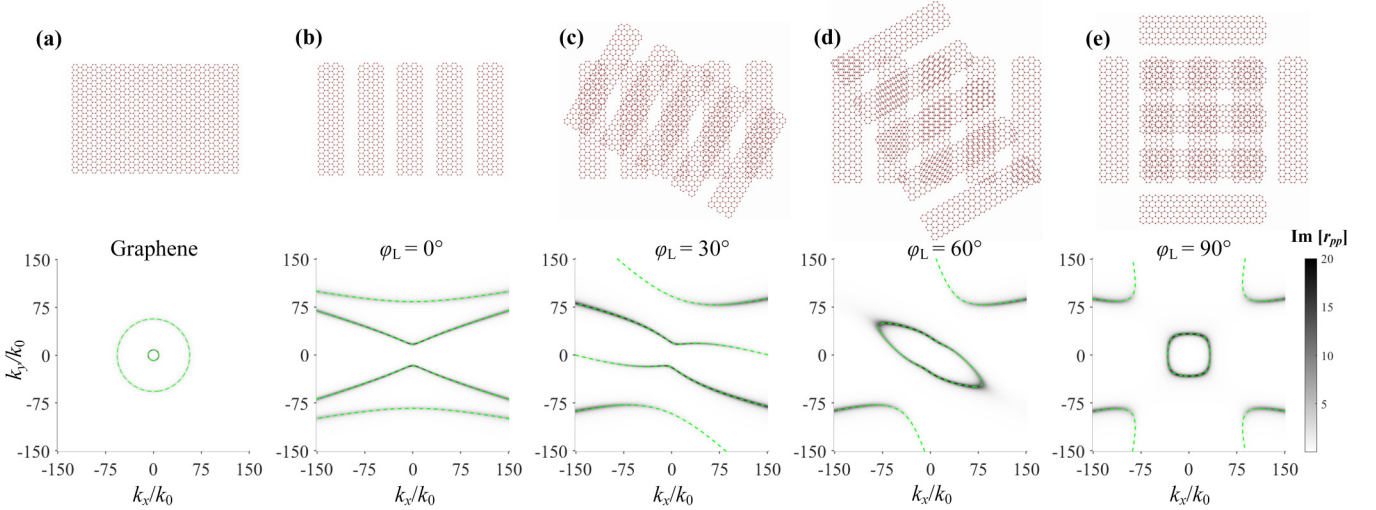


FIG. 3. Twist-induced topological transition of hyperbolic surface plasmon polaritons (HSPPs). (a)–(e) The upper panel shows the formed twisted fringe patterns of the twisted bilayered system. The bottom panel shows the corresponding contours of the imaginary part of the reflection coefficient, viz., $\text{Im}[r_{pp}]$, in the wave vector space at a frequency of $\omega_{\text{res}} = 1.756 \times 10^{14}$ rad/s. The parameters are set as $d_G = 10$ nm, $\mu = 0.5$ eV, $W = 10$ nm, $f = 0.5$, and $\varepsilon_d = 1$.

We can see that, in most cases, compared with the vacuum case, the presence of GS significantly amplifies h between nanoparticles, but in most cases, it is smaller than that in the presence of the bilayered unpatterned graphene sheets, which is shown by the orange dot-and-dash line in Fig. 4. We emphasize that when two nanoparticles are brought in proximity to the surface, due to the excitation of hybrid HSPPs, the amplification in h is mainly due to the enhancement of the electromagnetic field on the GS. The hybrid HSPPs propagate along the surface and couple with the free-space propagating waves emitted by the nanoparticles, thus providing an

additional channel for energy transmission between nanoparticles. In addition, we noted that HTC is smaller than that in vacuum when φ_L is at specific angles. This is because the bilayered GS can couple and guide the free-space waves emitted by nanoparticles, and the propagation direction of free-space waves can be effectively controlled through an interlayer twist. When the direction of nanoparticle arrangement does not match with the direction of free-space waves, HTC will be suppressed, even less than that in the case of vacuum [38].

Note that the total HTC is the integration of the spectral HTC by the relation of $h = \int_0^\infty h(\omega) d\omega$. Figure 5(a) gives the spectral HTC $h(\omega_{\text{res}})$ at the nanoparticle resonance of $\omega_{\text{res}} = 1.756 \times 10^{14}$ rad/s for the geometries, as shown in Fig. 1(a). We see that the trends of $h(\omega_{\text{res}})$ are almost the same as those for the total HTC. The distributions of the spectral HTC $h(\omega)$ vs the frequency and the interlayer twist of GS2 are presented in Figs. 5(b) and 5(c), respectively. It is observed that the brightest regions emerge at the nanoparticle resonance for all cases, which indicates that the HTC for SiC nanoparticles is dominated at the nanoparticle resonance. This is consistent with the results of previous work [30,31]. Moreover, we see that with increasing interlayer twisted angle, $h(\omega)$ shows a higher value around resonance frequency ranges. In a larger range of φ_L , spectral HTC for the case of bilayered unpatterned graphene sheets is larger than that of the bilayered GS. With further increasing φ_L to a value approaching 90° , the value and range of the bright region of $h(\omega)$ above the bilayered GS are larger than that above the bilayered unpatterned graphene sheets, as shown in Figs. 5(b) and 5(c), which makes the HTC for the case of GS larger than that of unpatterned graphene sheets, as depicted in Fig. 5(a). To focus on the physical phenomenon and save the computation resources, we only calculate the spectral HTC at ω_{res} in the following.

Figure 5 shows that, when the interlayer twisted angle is small, i.e., 0° , $h(\omega_{\text{res}})$ increases as the filling factor increases. To further understand this phenomenon, we plot the dispersion

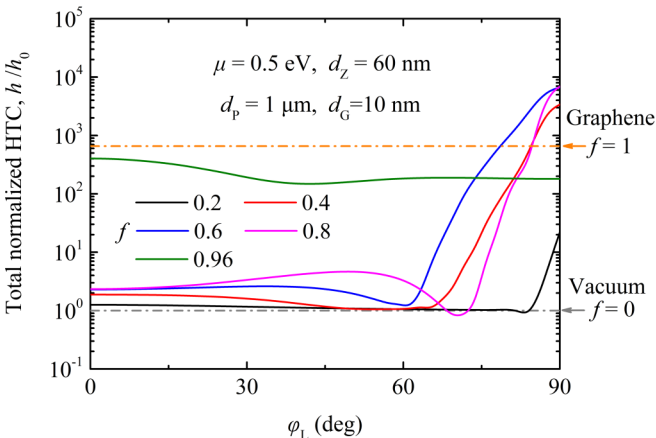


FIG. 4. Total normalized heat transfer conductance (HTC) h with respect to the interlayer twisted angle φ_L for different filling factors f . Normalization factor is the total HTC h_0 between nanoparticles without surface. The gray and orange dash-dot lines correspond to results in the case of vacuum and bilayered unpatterned graphene sheets. The SiC nanoparticles with an interparticle distance of $d_p = 1 \mu\text{m}$ are placed at a particle-surface distance of $d_z = 60$ nm above the twisted bilayered graphene strip (GS). The chemical potential of the GS is fixed at 0.5 eV.

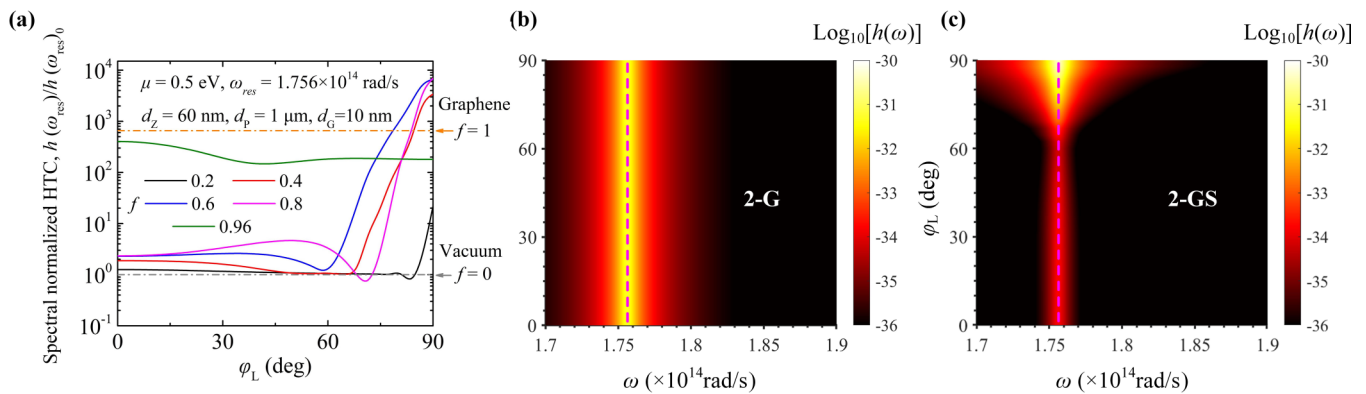


FIG. 5. (a) The spectral normalized heat transfer conductance (HTC) $h(\omega_{\text{res}})$ at $\omega_{\text{res}} = 1.756 \times 10^{14}$ rad/s with respect to the interlayer twisted angle φ_L for different filling factors f , normalized by the spectral HTC $h(\omega_{\text{res}})_0$ between nanoparticles without surface. The distributions of the spectral HTC vs the frequency and the interlayer twist for (b) the bilayered unpatterned graphene sheets and (c) the bilayered graphene strip (GS).

curve of the bilayered GS at different filling factors without twist ($\varphi_L = 0^\circ$) in Figs. 6(a) and 6(b). We notice that, when $f < 0.936$, the dispersion curve presents a hyperbolic topology (open), and as f increases, the large contrast between $\text{Im}[\sigma_{xx}^{\text{eff}}]$ and $\text{Im}[\sigma_{yy}^{\text{eff}}]$ makes the propagation of hybrid HSPPs more directional, and the symmetrical dispersion shrinks in the range of the wave vector. When f is low, the propagation distance of the large wave vector supported by symmetrical dispersion is very short, which makes it quickly dissipate. As f increases, the range of the wave vector supported by symmetrical dispersion decreases so that it can support heat

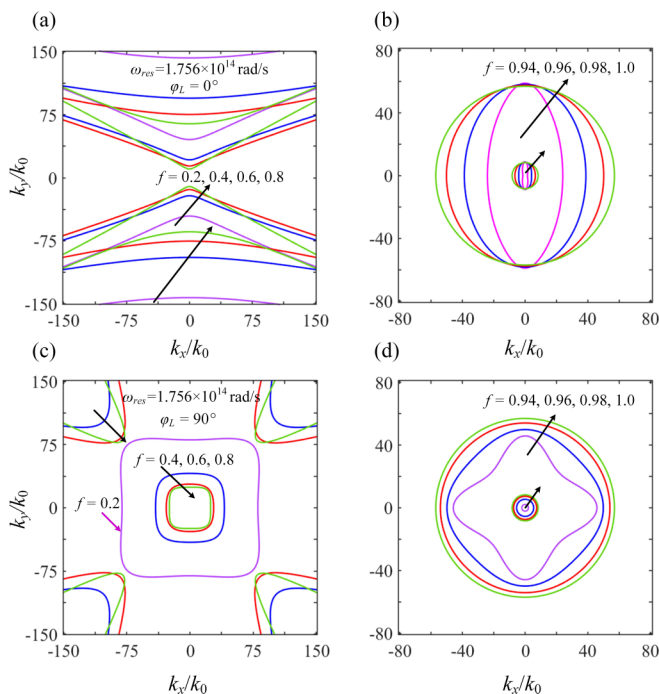


FIG. 6. The dispersion relations of the twisted bilayered graphene strip (GS) for different filling factors in the wave vector space at the interlayer twisted angle of (a) and (b) $\varphi_L = 0^\circ$ and (c) and (d) $\varphi_L = 90^\circ$ at $\omega_{\text{res}} = 1.756 \times 10^{14}$ rad/s. The parameters are $d_G = 10$ nm, $\mu = 0.5$ eV, $W = 10$ nm, $f = 0.5$, and $\varepsilon_d = 1$.

transfer between nanoparticles. This explains that, in the absence of an interlayer twist, the $h(\omega_{\text{res}})$ of nanoparticles increases as f increases, as observed in Fig. 5. When $f > 0.936$, since $\text{sgn}(\text{Im}[\sigma_{xx}^{\text{eff}}]) = \text{sgn}(\text{Im}[\sigma_{yy}^{\text{eff}}])$, the dispersion curves present an elliptical topology (closed); especially when $f = 1.0$, a circular topology is achieved. When $f < 0.936$, as the filling factors increase, the contrast between $\text{Im}[\sigma_{xx}^{\text{eff}}]$ and $\text{Im}[\sigma_{yy}^{\text{eff}}]$ increases, and the collimation and canalization of energy transmission become stronger. Since the nanoparticles are arranged perpendicular to the canalization direction, the heat transfer enhancement between the nanoparticles is negligible. When $f > 0.936$, especially when $f = 1.0$, the bilayered system supports the propagation of hybrid SPPs along the nanoparticle direction. At this time, the energy transmission between the two particles is significantly enhanced, which also explains the phenomenon that the $h(\omega_{\text{res}})$ reaches the maximum value as $f = 1.0$. When φ_L is large, especially at 90° , $h(\omega_{\text{res}})$ shows nearly four orders of magnitude enhancement compared with the case without a surface and even exceeds that of the case with the bilayered graphene sheets, as shown in Fig. 5. This can also be understood by the dispersion relationships obtained by Eq. (A8) as indicated in Figs. 6(c) and 6(d). It is shown that the dispersion curve shows a closed circumferencelike topology, which means that the propagation direction of hybrid HSPPs is no longer limited to the y direction, indicating a channel for the propagation of SPPs. Like that of the nontwisting case, when f increases, the system can support larger wave vector propagation, which gives rise to the increase in $h(\omega_{\text{res}})$, as shown in Fig. 5.

To illustrate the modulation effect of hybrid HSPPs induced by an interlayer twist on NFRHT between nanoparticles, two kinds of contours maps are shown in Figs. 7(a)–7(j) at ω_{res} . Figures 7(a)–7(e) show the real part of the reflected GF $\text{Re}[G_R(1, 1)]$ in the wave vector space in the case with the bilayered unpatterned graphene sheets or GS with interlayer twisted angles of 0° , 30° , and 90° , respectively. We observe that hybrid HSPPs are excited exactly at the dispersion curves. In the isotropic elliptical case (Fig. 7(a), $\text{Im}[\sigma_{xx}^{\text{eff}}] = \text{Im}[\sigma_{yy}^{\text{eff}}]$), the hybrid SPPs equally propagate in all directions along the surface, while in the hyperbolic case (Fig. 7(b), $\text{Im}[\sigma_{yy}^{\text{eff}}] \gg \text{Im}[\sigma_{xx}^{\text{eff}}]$), energy is strongly confined

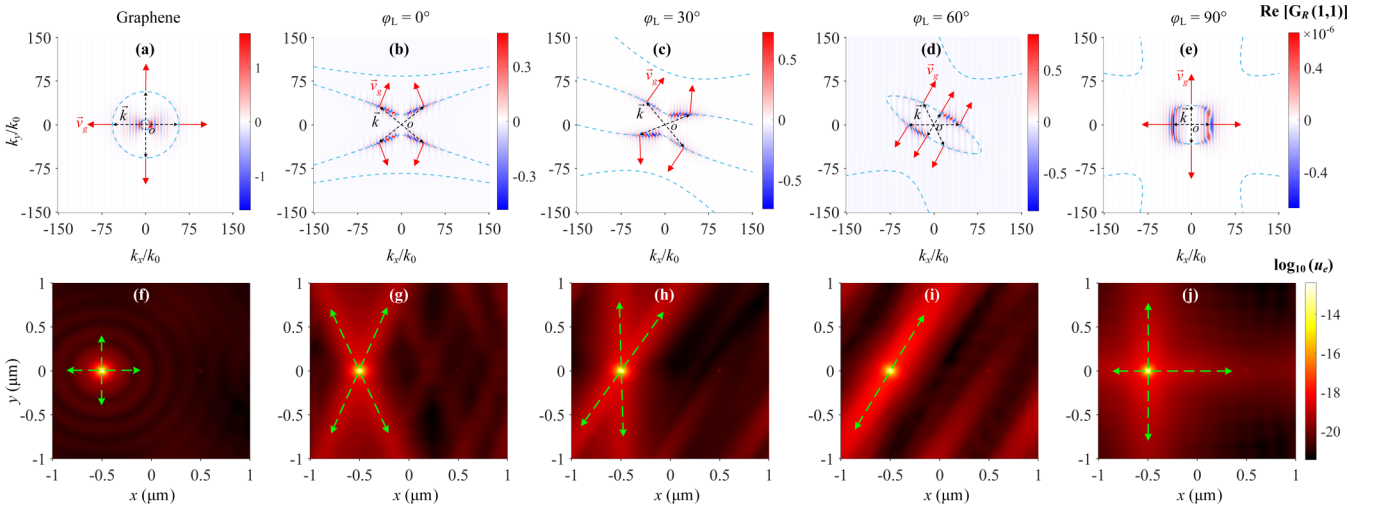


FIG. 7. (a)–(e) Wave vector contours of the real part of the first component of the reflected Green’s function (GF) $\text{Re}[G_R(1, 1)]$ for the case with unpatterned bilayered graphene sheets and bilayered graphene strips (GSs) at different interlayer twisted angles. Black dashed lines represent the polariton wave vectors, and red solid lines denote the group velocity directions. (f)–(j) Spatial contours of the electric field energy density U_e at $d_Z = 60$ nm corresponding to the cases in (a)–(e) at $\omega_{\text{res}} = 1.756 \times 10^{14}$ rad/s. In the upper panel, the blue dashed lines correspond to the isofrequency curves. For the bottom panel, the temperatures of the left and right nanoparticles are kept at 300 and 0 K, respectively. The green dashed arrow indicates the direction of maximum energy density. The parameters for these plots are $d_G = 10$ nm, $\mu = 0.5$ eV, $f = 0.5$, and $\varepsilon_d = 1.0$.

in specific directions. It has also clearly explained the topological transformation brought by the bilayered GS and the interlayer twist, thereby changing the propagation characteristics of the hybrid HSPPs, which confirms our qualitative discussions above.

Here, we adopt the graphical method from Refs. [19,38] to plot the directions of the group velocities ($\vec{v}_g = \nabla_{\vec{k}}\omega$) in Figs. 7(a)–7(e). The black dashed lines represent the polariton wave vectors, while the red solid lines denote the directions of the group velocity. We notice that the direction of the group velocity coincides with the direction of the strongest energy transfer of the nanoparticles, viz., the direction of the green dashed arrow in Figs. 7(f)–7(j). This is consistent with Refs. [19,38]. One can expect to have a large HTC when the interparticle axis is aligned with the direction of the group velocity. We observe that, for the bilayered graphene and the bilayered GS system with an interlayer twisted angle of 90° , the direction of group velocity is the same as the interparticle axis, thus greatly enhancing the heat transfer between the nanoparticles. For bilayered graphene sheets, the group velocity direction is distributed in all directions, while for the bilayered GS with an interlayer twisted angle of 90° , the group velocity is mainly distributed along two orthogonal directions, as shown by the red solid arrow in Fig. 7(e). This makes the energy transmission path of p_1 tightly bunched in two directions, resulting in the heat transfer between nanoparticles at this time larger than that of the bilayered graphene sheets. For the bilayered GS at interlayer twisted angles such as 0° and 30° , the enhancement of heat transfer between nanoparticles is not obvious because the group velocity direction does not match the interparticle axis. In addition, the different directions of group velocities lead to the strong transmission of energy along multiple directions. Near the interlayer twisted angle of $\varphi_L = 60^\circ$, hybrid HSPPs are highly

collimated, directive and diffractionless, as expected in the canalization regime with nearly fixed group velocity directions. Canalization supported by such band structure opens exciting opportunities for radiative energy transfer and enhanced local density of states.

Figures 7(f)–7(j) display the spatial distributions of the radiated electric field energy density obtained from [32]: $U_e(r, \omega) = (2\varepsilon_0^2/\pi\omega) \sum_j \chi_j \Theta(\omega, T_j) \text{Tr}[\mathbb{Q}_{rj} \mathbb{Q}_{rj}^*]$, where $\mathbb{Q}_{rj} = \omega^2 \mu_0 (\mathbf{G}_0^{rj} + \mathbf{G}_R^{rj}) \mathcal{G}$ and $\Theta(\omega, T_j) = \hbar\omega n(\omega, T)$ is the mean energy of the Planck oscillator at temperature T . We see that the case with the bilayered unpatterned graphene sheets exhibits much more homogeneous and evenly distribute energy in all directions, as sketched in Fig. 7(f). However, the presence of bilayered GS greatly modifies the energy distribution in the physical space, thus showing a unique inhomogeneity. In the case of bilayered GS without a twist, the higher energy density tends to be distributed along the green arrow, as shown in Fig. 7(g), which coincides with the direction of the bright band of GF in Fig. 7(b). We see that the energy emitted by p_1 is limited to some specific directions, which indicates that the collimation and channelization of energy transmission can be achieved by the bilayered GS. Owing to the mismatch between the connecting line between nanoparticles and the energy transmission direction, few SPPs directly make contribution to the heat transfer between the two nanoparticles. As a result, the enhancement of $h(\omega_{\text{res}})$ between the nanoparticles is weak. The above findings indicate that, for the bilayered GS, the particle energy is not transmitted most strongly along the strip direction but at a small angle. This direction corresponds to the bright area in the GF contour. This finding is consistent with the results in Refs. [18,19]. As the interlayer twisted angle increases, we notice that the angle between the green arrows gradually decreases. Especially for $\varphi_L = 60^\circ$, the isofrequency curve of the hybrid HSPPs undergoes

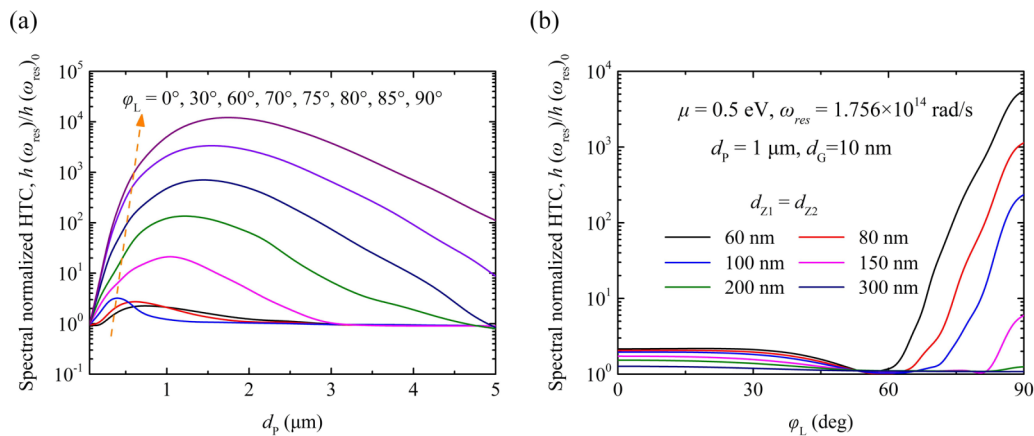


FIG. 8. (a) The spectral normalized heat transfer conductance (HTC) $h(\omega_{\text{res}})$ with respect to the interparticle distance d_p for different interlayer twisted angle φ_L . (b) The spectral HTC $h(\omega_{\text{res}})$ with respect to the interlayer twisted angle φ_L for different particle-interface distance d_z . The normalization factor is the spectral HTC $h(\omega_{\text{res}})_0$ between nanoparticles without surface. The parameters for these plots are $d_G = 10 \text{ nm}$, $\mu = 0.5 \text{ eV}$, $f = 0.5$, $\omega = \omega_{\text{res}}$, and $\varepsilon_d = 1.0$.

a topological transition. The propagation of hybrid HSPPs is strongly guided (canalization regime) along a specific direction without geometric spreading, and the energy transmission channel of p_1 is extremely limited, showing complete collimation and unidirectional canalization, as depicted in Fig. 7(i). However, since the energy transmission direction is not aligned with the x axis, the $h(\omega_{\text{res}})$ between p_1 and p_2 is still relatively small, while compared with a smaller interlayer twisted angle, i.e., 0° and 30° , more energy is transferred to the p_2 for $\varphi_L = 60^\circ$. When the interlayer twisted angle is further increased, viz., 90° , GS1 and GS2 are arranged orthogonally. We observe that the canalization effect of energy transmission disappears, and a direct propagation of the hybrid HSPPs along the x axis is established, hence a large energy density distributed along the x axis. These physics give an interpretation for the effect of the topological transition induced by the interlayer twist on $h(\omega_{\text{res}})$ between nanoparticles, as shown in Fig. 5. The topology transition of the hybrid HSPPs can entail a dramatic increase in the local density of states. Nevertheless, due to the weak coupling SPPs between adjacent GS with a small filling factor, this enhancement of $h(\omega_{\text{res}})$ cannot be achieved at any twisted angle, i.e., $f = 0.2$ in Fig. 5.

We now address the question of the dependence of the HTC on the distances. We stress that there are two distances in our configuration, viz., the interparticle distance d_p and the particle-surface distance d_z . It is expected that the first distance d_p is a relevant parameter to highlight the propagation characteristics of the hybrid HSPPs along the surface. Since the surface waves are evanescent waves with amplitudes decreasing away from the interface on a scale of one wavelength, we thus expect that the dependence of the second distance d_z could be used to elucidate the tunneling effects in our configuration.

The results of $h(\omega_{\text{res}})$ with respect to the first distance d_p are presented in Fig. 8(a). We plot the normalized $h(\omega_{\text{res}})$ [where normalized factor is the $h(\omega_{\text{res}})$ between the two nanoparticles without the surface] as a function of d_p . The nonmonotonous characteristics are observed in these curves, indicating that a maximum HTC can be obtained at a specific interparticle distance. For instance, $h(\omega_{\text{res}})$ reaches a

maximum value at $d_p = 1.70 \mu\text{m}$ for $\varphi_L = 90^\circ$ and at $d_p = 0.36 \mu\text{m}$ for $\varphi_L = 60^\circ$.

Now we turn our attention to elucidate the effect of the second distance d_z . Figure 8(b) shows the normalized spectral HTC at ω_{res} . We see that an enhancement of more than three orders of magnitude is achieved in the near field. As d_z increases from near to far field, due to the decreasing amplitude of the tunneling evanescent waves, the heat fluxes converge to the one in the absence of the surface. The enhancement or suppression of heat transfer provided by the bilayered GS is negligible in the far field.

We adopt the propagation length and decay length to interpret the above trends observed in Fig. 8. The propagation length of the hybrid HSPPs, viz., $L = 1/\text{Im}(K)$, can be comparable with one or several wavelengths. Here, K is the resonant parallel wave vector, determined by the dispersion relations of the surface. Based on the physical meaning of L , we can thus expect that, in the range of $d_p < L$, the hybrid HSPPs excited by p_1 could propagate to the position below p_2 with a big amplitude, subsequently tunneling into it. However, we can expect that, since the supported hybrid HSPPs are anisotropic, the propagation length of the SPPs supported by the bilayered GS varies with the directions. We find L by calculating the dispersion relations of the bilayered GS. In Fig. 9(a), we give the definition of the propagation direction of the hybrid HSPPs excited ϕ_{PL} directional wave. The results at ω_{res} for the bilayered twisted system at different directions ϕ_{PL} are presented in Fig. 9(b). Not surprisingly, we see that the propagation length is valid only at a limited range of directions. A comparison between Figs. 8(a) and 9(b) gives the fact that the maximum HTC at an interparticle distance d_p can be approximately consistent with the propagation length of the hybrid HSPPs modes. For instance, for $\varphi_L = 90^\circ$, the polariton propagation length along the interparticle axis is $1.61 \mu\text{m}$. We thus observe a peak value at $d_p \approx 1.70 \mu\text{m}$ on the curve for $\varphi_L = 90^\circ$, as shown in Fig. 8(a), while interpreting the trend as shown in Fig. 8(b), we plot in Fig. 9(c) the SPP decay length $\delta = 1/\text{Im}(k_z)$ at ω_{res} in the direction perpendicular to the bilayered system in the vacuum. We see that the decay length curves exhibit the same trends as those of the

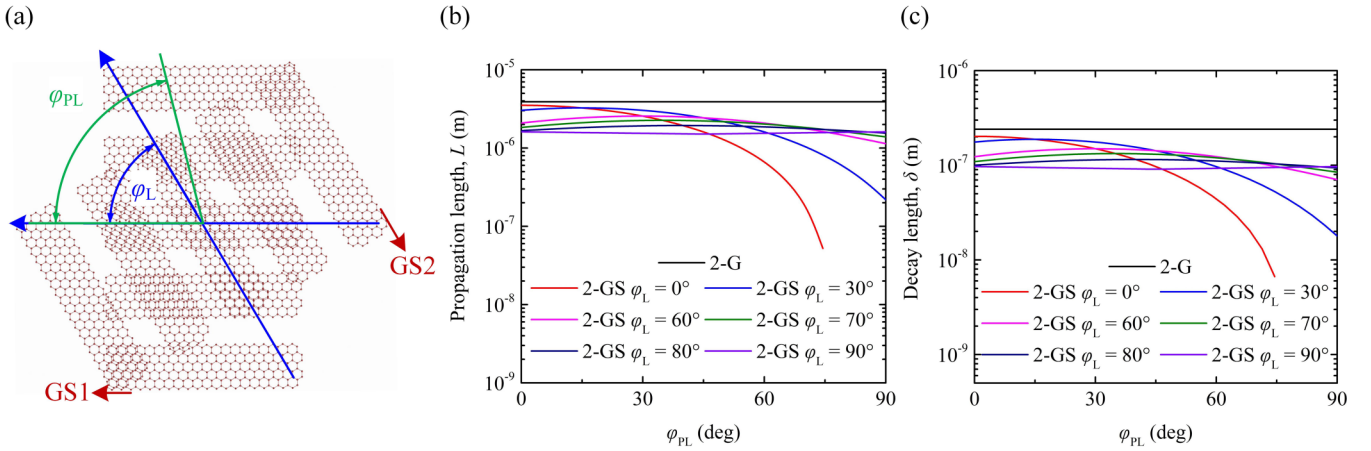


FIG. 9. (a) Definition of the propagation direction of the hybrid hyperbolic surface plasmon polaritons (HSPPs) excited at an angle of φ_{PL} . (b) Propagation length of the hybrid HSPPs along the surface at ω_{res} calculated from $L = 1/\text{Im}(K)$ in different directions. (c) Decay length of the hybrid HSPPs along the z direction at ω_{res} calculated from $\delta = 1/\text{Im}(k_z)$ in different directions. The parameters for these plots are $d_G = 10$ nm, $\mu = 0.5$ eV, $f = 0.5$, and $\varepsilon_d = 1.0$.

propagation lengths in Fig. 9(b). Thus, as shown in Fig. 8(b), when $\varphi_L = 90^\circ$ and d_Z is small, the heat transfer between nanoparticles shows a significant enhancement. However, when d_Z increases to a larger value, i.e., $d_Z = 100$ nm, the heat transfer enhancement of nanoparticles is negligible.

V. COMBINED EFFECT OF INTERLAYER TWIST AND INTEGRAL TWIST

Up to now, we have discussed only the case that the α axis is coincident with the x axis. We note that, under different arrangement directions of the bilayered GS, due to the anisotropic SPPs induced by the hybrid HSPPs, the interaction between the nanoparticles and the bilayered GS exhibits a huge difference. We can thus expect that a significant impact on NFRHT between the nanoparticles can be achieved. As shown in Fig. 10, we keep the positions of the nanoparticles unchanged while we do two kinds of rotation operations on the bilayered GS. We give the GS1 a twisted angle φ_B with respect to the x axis, which we name the integral twisted angle of the bilayered GS, and then rotate the GS2 relative to GS1 at an interlayer twisted angle of φ_L . The other parameters are the same as those used in Fig. 10. We define the modulation ratio as $\eta(\phi) = h(\omega)_\phi/h(\omega)_0$, which is a parameter for measuring modulation effect. It has been found that, when two nanoparticles are placed on monolayer graphene with a magnetic field applied on it, the HTC between nanoparticles can be regulated within a range of two orders of magnitude [35]. In addition, when the nanoparticles are placed on the hBN plate, the HTC between the nanoparticles can be regulated within a range of more than three orders of magnitude by twisting the optical axis of the hBN [38].

In Fig. 11, we show the ratio η between the spectral conductance $h(\omega_{res})$ of the configuration in the presence of bilayered GS and the one in the presence of bilayered unpatterned graphene sheets with different interlayer twisted angle φ_L (0° – 90°) and integral twisted angle φ_B (0° – 180°) at an interparticle distance of 0.5 or 1.0 μm . The green dashed line corresponds to the maximum η for different φ_L . We

notice that, under different interlayer twist conditions, the maximum value of η appears near an integral twisted angle of 60° . Moreover, we also find that, under the combined effect of interlayer and integral twist conditions, the coupling of nanoparticles with hybrid HSPPs in different directions shows huge differences. The heat transfer between nanoparticles can be regulated within a range of five orders of magnitude and can be either higher or much lower than that of the bilayered unpatterned graphene sheets. We also notice that, with the increase of the interparticle distance, the enhancement range of the hybrid HSPPs on the nanoparticles is more significant.

To interpret the underlying physics of the effect of the combined twist on NFRHT between nanoparticles, we show

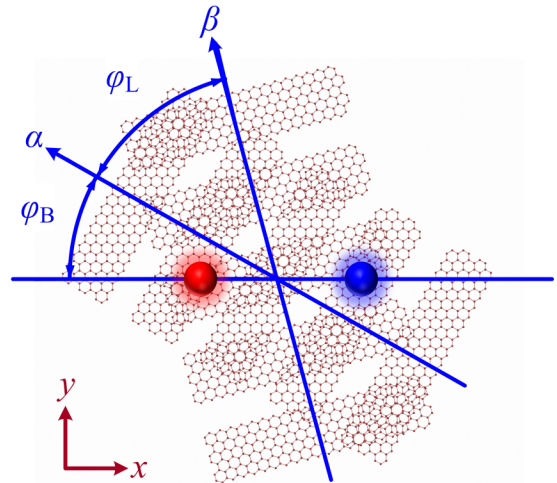


FIG. 10. Schematic of near-field radiative heat transfer (NFRHT) between two nanoparticles separated by an interparticle distance of d_p above the twisted bilayered system. φ_B and φ_L denote the integral twisted angle of the bilayered graphene strip (GS) relative to the two nanoparticles, and the interlayer twisted angle of GS2 relative to GS1, respectively. The twist of the GS is executed clockwise. The connecting line between nanoparticles p_1 – p_2 is aligned with the x axis.

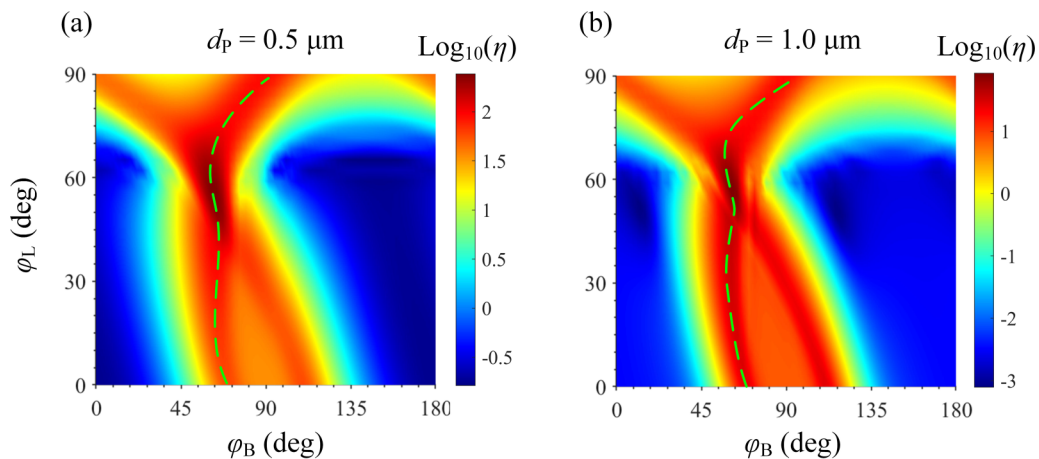


FIG. 11. The ratio between the spectral conductance $h(\omega_{\text{res}})$ of the configuration in the presence of bilayered graphene strip (GS) and the one in the presence of bilayered graphene as a function of integral twisted angle φ_B and interlayer twisted angle φ_L at an interparticle distance of (a) $0.5 \mu\text{m}$ and (b) $1.0 \mu\text{m}$. The green dashed line corresponds to the maximum spectral conductance at different φ_B and φ_L . The parameters are set as $d_Z = 60 \text{ nm}$, $d_G = 10 \text{ nm}$, $\mu = 0.5 \text{ eV}$, $f = 0.5$, and $\varepsilon_d = 1$.

in Figs. 12(a)–12(h) the spatial distributions of the electric field energy density for several cases with different twisted arrangements of (φ_L, φ_B) . The strongest transmission along the two specific directions is shown by the green arrow in the Fig. 12. We first consider the case where there is no interlayer twist ($\varphi_L = 0^\circ$), which means that GS1 and GS2 twist synchronously with respect to the nanoparticles. We see that the energy transmission path presents a hyperbolic topology. With the increase of the φ_B , the direction of high energy density gradually approaches the particle arrangement direction and almost coincides with the line of p_1-p_2 at $\varphi_B = 60^\circ$, where the energy density of p_2 reaches its peak. As φ_B further increases, the green arrow direction will move away from the line of p_1-p_2 ; hence, a decrease in the energy density of

p_2 is observed. This is consistent with the results shown in Fig. 11. For the case of $\varphi_L = 60^\circ$ in the lower panel of Fig. 12, we observe that the energy transmission channel is extremely confined, showing complete collimation and unidirectional canalization. The strongest energy is directed toward one specific direction denoted by the green arrow. When $\varphi_B = 0^\circ$, the energy canalization direction does not match the connecting line p_1-p_2 . With the increase of φ_B , the canalization direction and the connecting line p_1-p_2 get closer. Especially when the green arrow is aligned with the x axis at $\varphi_B = 60^\circ$, the energy density of p_2 reaches the maximum. We can thus conclude that the combination of interlayer twist and integral twist of the GS can make the energy transmission converge in a specific direction to achieve the canalization of the energy

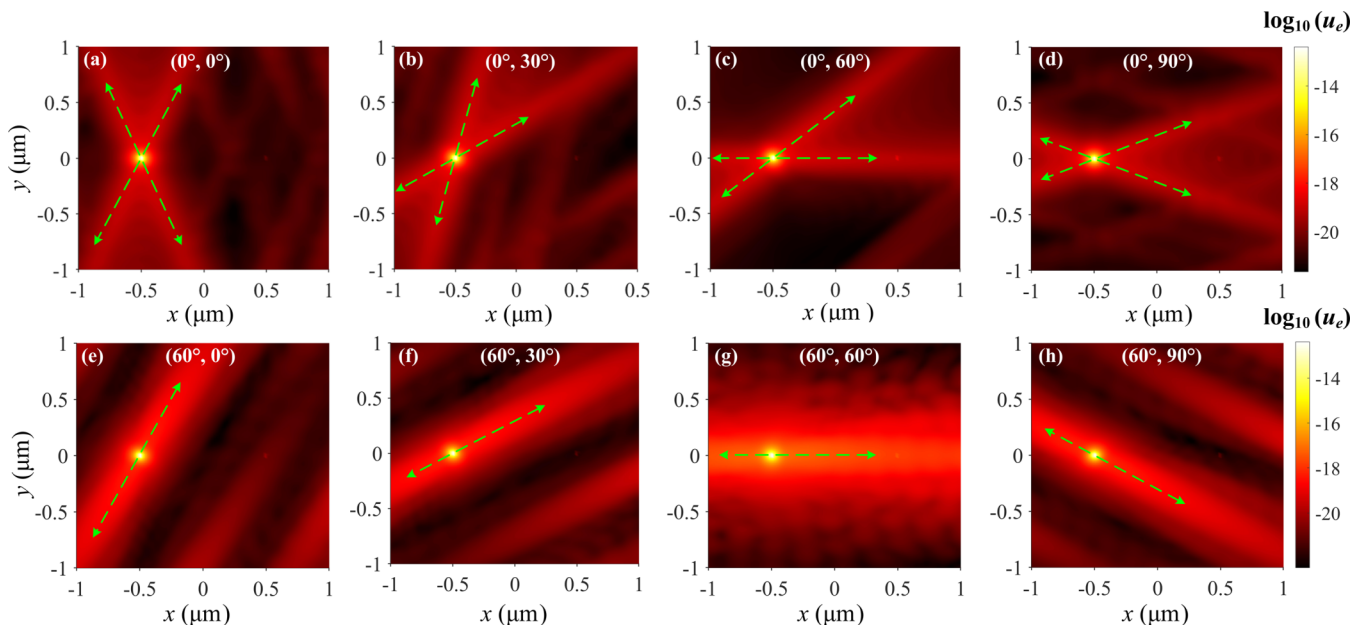


FIG. 12. The spatial contours of the electric field energy density U_e of the bilayered graphene strip (GS) at $\omega_{\text{res}} = 1.756 \times 10^{14} \text{ rad/s}$ under different interlayer twisted angles and integral twisted angles, viz., (φ_L, φ_B) . The parameters are set as $d_Z = 60 \text{ nm}$, $d_G = 10 \text{ nm}$, $\mu = 0.5 \text{ eV}$, $f = 0.5$, and $\varepsilon_d = 1$.

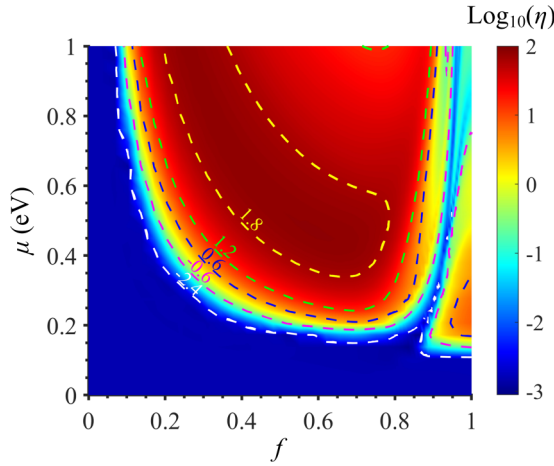


FIG. 13. The ratio between the spectral conductance $h(\omega_{\text{res}})$ of the configuration in the presence of bilayered graphene strip (GS) and the one in the presence of bilayered graphene as a function of the filling factor f and the chemical potential μ of the bilayered GS at an interparticle distance of $1.0 \mu\text{m}$. The parameters are set as $\varphi_L = \varphi_B = 60^\circ$, $d_Z = 60 \text{ nm}$, $d_G = 10 \text{ nm}$, and $\varepsilon_d = 1$.

transmission. Based on this fact, we can then flexibly enhance or suppress NFRHT between nanoparticles.

VI. EFFECT OF CHEMICAL POTENTIAL

It is well known that the chemical potential μ is an adjustable parameter allowing us to tune the optical properties of GS actively. There are several ways to modulate the chemical potential, such as using gates that can be placed far away from the grating system so as not to affect heat transfer or using nitric acid for chemical doping [55,56]. We expect that, by modulating μ of the GS, the NFRHT between the nanoparticles will be affected effectively. In the following calculations, the twisted angles of GS are chosen as $(\varphi_L, \varphi_B) = (60^\circ, 60^\circ)$, and the other parameters are the same as those used in Fig. 5.

To visualize the influence of μ , we plot the contour map of η as a function of μ and f in Fig. 13. We see that, with a small value of f , the influence of μ on $h(\omega_{\text{res}})$ is negligible. When f is large, viz., $0.1 < f < 0.936$, we observe that, as μ

increases, the η climbs and reaches the maximum value and then decreases, and when f is ~ 0.936 , there is an abrupt change of $h(\omega_{\text{res}})$. This is because when $f > 0.936$, the optical conductivity of GS has a sudden change, as shown in Fig. 2, and the propagation characteristics of hybrid HSPPs on it change greatly.

Figure 14 shows the real part of the first part of the GF and dispersion relations with a filling factor of 0.5 for different chemical potentials. We can see that, in the case of a small chemical potential of $\mu = 0.2 \text{ eV}$, the value of GF is much smaller than that of a large chemical potential. Under the condition of a large chemical potential, as the chemical potential further increases, the dispersion curves dominated by the antisymmetric dispersion shrink inward and support low- k modes, which also leads to the decrease of $h(\omega_{\text{res}})$.

VII. CONCLUSIONS

This paper presented the modification of NFRHT between two nanoparticles when a twisted bilayered GS system supporting hybrid HSPPs is placed nearby. The role of the propagation of hybrid HSPPs supported on a twisted bilayered structure composed of two GS on the heat transfer between nanoparticles is identified. As the interlayer twisted angle between the two GS increases, the surface state of the twisted bilayered system gradually changes from an open (hyperbolic) profile to a closed (elliptical) profile. With the emergence of the topological transformation of the hybrid HSPPs, the surface state becomes more intensive, leading to an enhancement in the NFRHT between the nanoparticles. Especially when the interlayer twisted angle is 60° , the hybridization of the HSPPs enables a complete collimation and unidirectional canalization of the energy transmission. By introducing an integral twisted angle of the bilayered GS, the strong anisotropy of surface plasmons propagating on twisted bilayered GS has been uncovered, and the couple between the energy of nanoparticles and hybrid HSPPs in different directions has been noticed. Furthermore, with the combined modulation of the interlayer and the integral twisted angles, five orders of magnitude control of NFRHT between nanoparticles can be achieved. Finally, we find that the chemical potential of the GS can be adjusted to effectively modulate the heat transfer in a large range. This paper represents a first step study of twisted

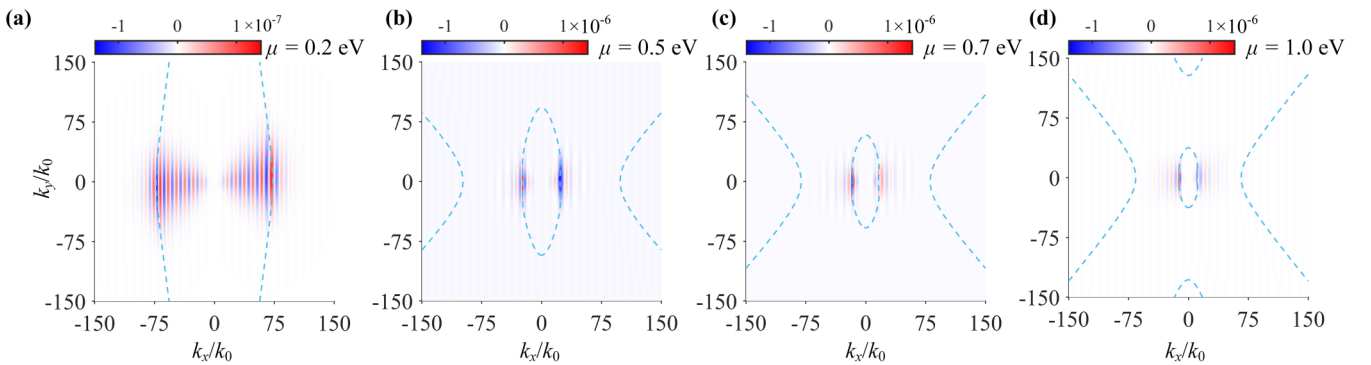


FIG. 14. Wave vector contours of the real part of the first component of the reflected Green's function (GF) $\text{Re}[G_R(1, 1)]$ at a chemical potential of (a) 0.2 eV, (b) 0.5 eV, (c) 0.7 eV, and (d) 1.0 eV. The blue dashed line corresponds to the dispersion relations of the hybrid hyperbolic surface plasmon polaritons (HSPPs). The parameters are set as $d_G = 10 \text{ nm}$, $d_Z = 60 \text{ nm}$, and $f = 0.5$.

physics-mediated energy exchange and provides a hybridization effect of polaritons on NFRHT between nanoparticles.

ACKNOWLEDGMENTS

Yong Zhang acknowledges the support of the National Natural Science Foundation of China (Grant No. 52076056). Hong-Liang Yi acknowledges the Fundamental Research Funds for the Central Universities (Grant No. AUGA5710094020).

$$\hat{\sigma}'' = \begin{pmatrix} \sigma''_{xx} & \sigma''_{xy} \\ \sigma''_{yx} & \sigma''_{yy} \end{pmatrix} = \frac{1}{k^2} \begin{bmatrix} k_x^2 \sigma_{xx} + k_y^2 \sigma_{yy} + k_x k_y (\sigma_{xy} + \sigma_{yx}) & k_x^2 \sigma_{xy} - k_y^2 \sigma_{yx} + k_x k_y (\sigma_{yy} - \sigma_{xx}) \\ k_x^2 \sigma_{yx} - k_y^2 \sigma_{xy} + k_x k_y (\sigma_{yy} - \sigma_{xx}) & k_x^2 \sigma_{yy} + k_y^2 \sigma_{xx} - k_x k_y (\sigma_{xy} + \sigma_{yx}) \end{bmatrix}. \quad (\text{A1})$$

Under the combined effect of the interlayer twisted angle φ_L and integral twisted angle φ_B , the anisotropic conductivity with respect to the unit vector of k_ρ is given by $R' \hat{\sigma}'' R$, where $R' = \begin{bmatrix} \cos(\varphi_L + \varphi_B) & \sin(\varphi_L + \varphi_B) \\ -\sin(\varphi_L + \varphi_B) & \cos(\varphi_L + \varphi_B) \end{bmatrix}$ and $R = \begin{bmatrix} \cos(\varphi_L + \varphi_B) & -\sin(\varphi_L + \varphi_B) \\ \sin(\varphi_L + \varphi_B) & \cos(\varphi_L + \varphi_B) \end{bmatrix}$. Note that we do two kinds of clockwise rotation operations on the bilayered GS while keeping the position of the nanoparticles unchanged. Following Refs. [57–59], let us write the EM fields of the s -polarized transverse electric (TE) and p -polarized transverse magnetic (TM) components of the EM wave separately and then mix them with the nondiagonal response of the metasurface. The s waves with the electric field perpendicular to the plane of incidence possess the EM field components $E_s = \{0, E_y, 0\}$, $H_s = \{H_x, 0, H_z\}$. For the p waves, with the magnetic field perpendicular to the plane of incidence, the EM field components are $E_p = \{E_x, 0, E_z\}$, $H_p = \{0, H_y, 0\}$. Substituting the boundary conditions of s and p waves at the metasurface, one obtains the 4×4 T-matrix, which gives the relation between all the electric field components in the media above and below the metasurface [60–62]:

$$\begin{pmatrix} H_{p1}^+ \\ H_{p1}^- \\ E_{s1}^+ \\ E_{s1}^- \end{pmatrix} = \hat{T}_{1 \rightarrow 2} \begin{pmatrix} H_{p2}^+ \\ H_{p2}^- \\ E_{s2}^+ \\ E_{s2}^- \end{pmatrix} = \begin{pmatrix} T_{11} & T_{12} & T_{13} & T_{14} \\ T_{21} & T_{22} & T_{23} & T_{24} \\ T_{31} & T_{32} & T_{33} & T_{34} \\ T_{41} & T_{42} & T_{43} & T_{44} \end{pmatrix} \begin{pmatrix} H_{p2}^+ \\ H_{p2}^- \\ E_{s2}^+ \\ E_{s2}^- \end{pmatrix}. \quad (\text{A2})$$

Here, the signs of + and – represent forward and backward waves, respectively. Also, $\hat{T}_{1 \rightarrow 2}$ can be defined as

$$\hat{T}_{1 \rightarrow 2} = \frac{1}{2} \begin{bmatrix} \frac{k_{z2}}{\epsilon_2} \begin{pmatrix} P_{12}^{++} & P_{12}^{+-} \\ P_{12}^{-+} & P_{12}^{--} \end{pmatrix} & \sqrt{\frac{\mu_0}{\epsilon_0}} \sigma_{xy}'' \begin{pmatrix} 1 & 1 \\ 1 & 1 \end{pmatrix} \\ \sqrt{\frac{\mu_0}{\epsilon_0}} \frac{k_{z2} \mu_1}{k_{z1} \epsilon_2} \sigma_{yx}'' \begin{pmatrix} 1 & -1 \\ -1 & 1 \end{pmatrix} & \frac{\mu_1}{k_{z1}} \begin{pmatrix} S_{12}^{++} & S_{12}^{+-} \\ S_{12}^{-+} & S_{12}^{--} \end{pmatrix} \end{bmatrix}, \quad (\text{A3})$$

where the p -wave components are

$$\begin{aligned} P_{12}^{++} &= \frac{\epsilon_1}{k_{z1}} + \frac{\epsilon_2}{k_{z2}} + \frac{\sigma''_{xx}}{\omega \epsilon_0}, & P_{12}^{-+} &= -\frac{\epsilon_1}{k_{z1}} + \frac{\epsilon_2}{k_{z2}} - \frac{\sigma''_{xx}}{\omega \epsilon_0}, \\ P_{12}^{+-} &= -\frac{\epsilon_1}{k_{z1}} + \frac{\epsilon_2}{k_{z2}} + \frac{\sigma''_{xx}}{\omega \epsilon_0}, & P_{12}^{--} &= \frac{\epsilon_1}{k_{z1}} + \frac{\epsilon_2}{k_{z2}} - \frac{\sigma''_{xx}}{\omega \epsilon_0}, \end{aligned} \quad (\text{A4})$$

APPENDIX A: THE REFLECTION MATRIX OF THE BILAYERED ANISOTROPIC METASURFACES

A generalized 4×4 T-matrix formalism for arbitrary anisotropic 2D layers is adopted to obtain the reflection matrix in our calculations. Let us firstly consider a single anisotropic metasurface at the interface between two semi-infinite media with refractive indexes of $n_1 = \sqrt{\epsilon_1 \mu_1}$ and $n_2 = \sqrt{\epsilon_2 \mu_2}$. Within the homogenization approach, the electromagnetic (EM) response of the metasurface, in general, can be described by a fully populated conductivity tensor $\hat{\sigma}''$ in the wave vector space [37,54]:

and the s -wave components are given by

$$\begin{aligned} S_{12}^{++} &= \frac{k_{z1}}{\mu_1} + \frac{k_{z2}}{\mu_2} + \omega \mu_0 \sigma''_{yy}, & S_{12}^{-+} &= \frac{k_{z1}}{\mu_1} - \frac{k_{z2}}{\mu_2} + \omega \mu_0 \sigma''_{yy}, \\ S_{12}^{+-} &= \frac{k_{z1}}{\mu_1} - \frac{k_{z2}}{\mu_2} - \omega \mu_0 \sigma''_{yy}, & S_{12}^{--} &= \frac{k_{z1}}{\mu_1} + \frac{k_{z2}}{\mu_2} - \omega \mu_0 \sigma''_{yy}. \end{aligned} \quad (\text{A5})$$

For the monolayer anisotropic metasurface, the reflection matrix \mathbf{R}_m is defined and expressed in terms of the T-matrix elements as follows [63]:

$$\begin{aligned} r_{pp} &= \frac{T_{21} T_{33} - T_{23} T_{31}}{T_{11} T_{33} - T_{13} T_{31}}, & r_{ps} &= \frac{T_{41} T_{33} - T_{43} T_{31}}{T_{11} T_{33} - T_{13} T_{31}}, \\ r_{sp} &= \frac{T_{11} T_{23} - T_{13} T_{21}}{T_{11} T_{33} - T_{13} T_{31}}, & r_{ss} &= \frac{T_{11} T_{43} - T_{13} T_{41}}{T_{11} T_{33} - T_{13} T_{31}}. \end{aligned} \quad (\text{A6})$$

The formalism developed above can be easily generalized for an arbitrary number of layers by multiplying the T-matrices corresponding to each layer. For a bilayered metasurface with an effective conductivity tensor of $\hat{\sigma}_i''$ ($i = 1, 2$), the total T-matrix is given by $\hat{T}_{1 \rightarrow N} = \hat{T}_{1 \rightarrow 2} \hat{T}_{d_1} \hat{T}_{2 \rightarrow 3}$, where $\hat{T}_{2 \rightarrow 3}$ is obtained from $\hat{T}_{1 \rightarrow 2}$ by replacing media $\epsilon_{1,2}$ with $\epsilon_{2,3}$. \hat{T}_{d_1} is the T matrix for a wave propagating through the interlayers (media between two adjacent 2D layers) with a corresponding thickness of d_G :

$$\hat{T}_{d_1} = \begin{pmatrix} e^{-ik_{z1} d_G} & 0 & 0 & 0 \\ 0 & e^{ik_{z1} d_G} & 0 & 0 \\ 0 & 0 & e^{-ik_{z1} d_G} & 0 \\ 0 & 0 & 0 & e^{ik_{z1} d_G} \end{pmatrix}. \quad (\text{A7})$$

The dispersion of coupled hybrid HSPPs can be obtained as zeros of the denominator of the reflection coefficients:

$$T_{11} T_{33} - T_{13} T_{31} = 0. \quad (\text{A8})$$

The T-matrix allows us to obtain all necessary characteristics (the reflection and the dispersion relation) using general Eqs. (A2)–(A7).

- [1] T. Kralik, P. Hanzelka, M. Zobac, V. Musilova, T. Fort, and M. Horak, *Phys. Rev. Lett.* **109**, 224302 (2012).
- [2] S.-A. Biehs, M. Tschikin, R. Messina, and P. Ben-Abdallah, *Appl. Phys. Lett.* **102**, 131106 (2013).
- [3] S.-A. Biehs, M. Tschikin, R. Messina, and P. Ben-Abdallah, *Phys. Rev. Lett.* **109**, 104301 (2012).
- [4] D. Polder and M. Van Hove, *Phys. Rev. B* **4**, 3303 (1971).
- [5] S. V. Boriskina, J. K. Tong, Y. Huang, J. W. Zhou, V. Chiloyan, and G. Chen, *Photonics*, **2**, 659 (2015).
- [6] K. Joulain, J. P. Mulet, F. Marquier, R. Carminati, and J. J. Greffet, *Surf. Sci. Rep.* **57**, 59 (2005).
- [7] S. Shen, A. Narayanaswamy, and G. Chen, *Nano Lett.* **9**, 2909 (2009).
- [8] S. Z. Wen, X. L. Liu, S. Chen, Z. B. Wang, S. H. Zhang, and C. Z. Dang, *J. Quant. Spectrosc. Radiat. Transfer.* **234**, 1 (2019).
- [9] V. Kubyt'skiy, S.-A. Biehs, and P. Ben-Abdallah, *Phys. Rev. Lett.* **113**, 074301 (2014).
- [10] R. Messina and P. Ben-Abdallah, *Sci. Rep.* **3**, 1383 (2013).
- [11] X. L. Liu and Z. M. Zhang, *Appl. Phys. Lett.* **107**, 143114 (2015).
- [12] M. J. He, H. Qi, Y. T. Ren, Y. J. Zhao, and M. Antezza, *Int. J. Heat Mass Transfer.* **150**, 119305 (2020).
- [13] J. D. Shen, S. Guo, X. L. Liu, B. A. Liu, W. T. Wu, and H. He, *Appl. Therm. Eng.* **144**, 403 (2018).
- [14] C. L. Zhou, S. H. Yang, Y. Zhang, and H. L. Yi, *Nanosc. Microsc. Therm.* **24**, 168 (2020).
- [15] O. Y. Yermakov, A. I. Ovcharenko, M. Song, A. A. Bogdanov, I. V. Iorsh, and Yu. S. Kivshar, *Phys. Rev. B* **91**, 235423 (2015).
- [16] A. A. High, R. C. Devlin, A. Dibos, M. Polking, D. S. Wild, J. Perczel, N. P. de Leon, M. D. Lukin, and H. Park, *Nature (London)* **522**, 192 (2015).
- [17] J. S. Gomez-Diaz, M. Tymchenko, and A. Alù, *Phys. Rev. Lett.* **114**, 233901 (2015).
- [18] G. W. Hu, A. Krasnok, Y. Mazor, C. W. Qiu, and A. Alu, *Nano Lett.* **20**, 3217 (2020).
- [19] G. W. Hu, Q. D. Ou, G. Y. Si, Y. J. Wu, J. Wu, Z. G. Dai, A. Krasnok, Y. Mazor, Q. Zhang, Q. L. Bao, C. W. Qiu, and A. Alu, *Nature (London)* **582**, 209 (2020).
- [20] J. H. Duan, N. Capote-Robayna, J. Taboada-Gutierrez, G. Alvarez-Perez, I. Prieto, J. Martin-Sanchez, A. Y. Nikitin, and P. Alonso-Gonzalez, *Nano Lett.* **20**, 5323 (2020).
- [21] Z. B. Zheng, F. S. Sun, W. C. Huang, J. Y. Jiang, R. Z. Zhan, Y. L. Ke, H. J. Chen, and S. Z. Deng, *Nano Lett.* **20**, 5301 (2020).
- [22] S. Carr, D. Massatt, S. Fang, P. Cazeaux, M. Luskin, and E. Kaxiras, *Phys. Rev. B* **95**, 075420 (2017).
- [23] F. C. Wu, T. Lovorn, and A. H. Macdonald, *Phys. Rev. Lett.* **118**, 147401 (2017).
- [24] V. Yannopapas and N. V. Vitanov, *Phys. Rev. Lett.* **110**, 044302 (2013).
- [25] J. Dong, J. Zhao, and L. Liu, *Phys. Rev. B* **95**, 125411 (2017).
- [26] M. G. Luo, J. Dong, J. M. Zhao, L. H. Liu, and M. Antezza, *Phys. Rev. B* **99**, 134207 (2019).
- [27] P. Ben-Abdallah, K. Joulain, J. Drevillon, and C. Le Goff, *Phys. Rev. B* **77**, 075417 (2008).
- [28] P. Ben-Abdallah, S.-A. Biehs, and K. Joulain, *Phys. Rev. Lett.* **107**, 114301 (2011).
- [29] K. Asheichyk and M. Kruger, *Phys. Rev. B* **98**, 195401 (2018).
- [30] Y. Zhang, M. Antezza, H. L. Yi, and H. P. Tan, *Phys. Rev. B* **100**, 085426 (2019).
- [31] Y. Zhang, H. L. Yi, H. P. Tan, and M. Antezza, *Phys. Rev. B* **100**, 134305 (2019).
- [32] J. Dong, J. Zhao, and L. Liu, *Phys. Rev. B* **97**, 075422 (2018).
- [33] R. Messina, S.-A. Biehs, and P. Ben-Abdallah, *Phys. Rev. B* **97**, 165437 (2018).
- [34] Y. Zhang, J. Dong, G. M. Tang, and H. L. Yi, *Phys. Rev. B* **103**, 195433 (2021).
- [35] M. J. He, Q. H., Y. X. Su, Y. T. Ren, Y. J. Zhao, and M. Antezza, *Appl. Phys. Lett.* **117**, 113104 (2020).
- [36] J. L. Fang, L. Qu, Y. Zhang, and H. L. Yi, *Phys. Rev. B* **102**, 245418 (2020).
- [37] J. S. Gomez-Diaz, M. Tymchenko, and A. Alù, *Opt. Mater. Express* **5**, 2313 (2015).
- [38] A. Ott, Y. Hu, X. H. Wu, and S.-A. Biehs, *Phys. Rev. Appl.* **15**, 064073 (2021).
- [39] P. J. van Zwol, S. Thiele, C. Berger, W. A. de Heer, and J. Chevrier, *Phys. Rev. Lett.* **109**, 264301 (2012).
- [40] P. J. van Zwol, L. Ranno, and J. Chevrier, *Phys. Rev. Lett.* **108**, 234301 (2012).
- [41] S. Shen, A. Mavrokefalos, P. Sambegoro, and G. Chen, *Appl. Phys. Lett.* **100**, 233114 (2012).
- [42] A. Narayanaswamy, S. Shen, and G. Chen, *Phys. Rev. B* **78**, 115303 (2008).
- [43] E. Rousseau, A. Siria, G. Jourdan, S. Volz, F. Comin, J. Chevrier, and J.-J. Greffet, *Nat. Photon.* **3**, 514 (2009).
- [44] S. Balci, A. Kocabas, C. Kocabas, and A. Aydinli, *Appl. Phys. Lett.* **98**, 031101 (2011).
- [45] E. Karademir, S. Balci, C. Kocabas, and A. Aydinli, *ACS Photon.* **2**, 805 (2015).
- [46] A. Espinha, C. Dore, C. Matricardi, M. I. Alonso, A. R. Goni, and A. Mihi, *Nat. Photon.* **12**, 343 (2018).
- [47] S. Albaladejo, R. Gómez-Medina, L. S. Froufe-Pérez, H. Marinchio, R. Carminati, J. F. Torrado, G. Armelles, A. García-Martín, and J. J. Sáenz, *Opt. Express* **18**, 3556 (2010).
- [48] L. Novotny and B. Hecht, *Principles of Nano-optics* (Cambridge University Press, Cambridge, 2012).
- [49] I. Latella, R. Messina, S.-A. Biehs, J. M. Rubi, and P. Ben-Abdallah, *Sci. Rep.* **10**, 8938 (2020).
- [50] A. Lakhatakia, *Int. J. Infrared Milli.* **13**, 161 (1992).
- [51] G. W. Hanson, *IEEE T. Antenn. Propag.* **56**, 747 (2008).
- [52] *Handbook of Optical Constants of Solids*, edited by E. Palik, (Academic, New York, 1998).
- [53] X. L. Liu, R. Z. Zhang, and Z. M. Zhang, *ACS Photon.* **1**, 785 (2014).
- [54] L. A. Falkovsky, *J. Phys. Conf. Ser.* **129**, 012004 (2008).
- [55] L. A. Falkovsky and S. S. Pershoguba, *Phys. Rev. B* **76**, 153410 (2007).
- [56] H. G. Hu, X. S. Li, B. Chandra, G. Tulevski, Y. Q. Wu, M. Freitag, W. J. Zhu, P. Avouris, and F. N. Xia, *Nat. Nanotechnol.* **7**, 330 (2012).
- [57] M. Nakayama, *J. Phys. Soc. Jpn.* **36**, 393 (1974).

- [58] K. W. Chiu and J. J. Quinn, *Phys. Rev. B* **9**, 4724 (1974).
- [59] O. V. Kotov and Y. E. Lozovik, *Phys. Rev. B* **100**, 165424 (2019).
- [60] T. Zhan, X. Shi, Y. Dai, X. Liu, and J. Zi, *J. Phys.: Condens. Matter* **25**, 215301 (2013).
- [61] C. L. Zhou, X. H. Wu, Y. Zhang, and H. L. Yi, *Phys. Rev. B* **103**, 155404 (2021).
- [62] C. L. Zhou, X. H. Wu, Y. Zhang, M. Xie, and H. L. Yi, *Appl. Phys. Lett.* **118**, 173103 (2021).
- [63] P. Yeh, *J. Opt. Soc. Am.* **69**, 742 (1979).